SSRG International Journal of Mechanical Engineering
ISSN: 2348-8360/ https://doi.org/10.14445/23488360/IJME-V13I7P109

Volume 13 Issue 7, 108-121, July 2026

Original Article

Optimizing Cylindrical Air Gap Membrane Distillation: A Random Forest Machine Learning Framework for Performance Analysis

Vandita Thantharate shahu[1], Prakash Dhopte[2], Arun Kose[3], Nitin Choudhary[4]

[1,3]*Ramdeobaba University, Nagpur, India.*
[2,4]*Jhulelal Institute of Technology, Nagpur, India.*

[1]*Corresponding Author : thantharatev@rknec.edu*

Received: 01 May 2026 Revised: 23 June 2026 Accepted: 08 Juy 2026 Published: 30 July 2026

Abstract *- The present study analyses the machine learning model of a Cylindrical Air Gap Membrane Distillation (CAGMD) system using a concentric PTFE membrane and copper condenser using a Random Forest (RF)-based machine learning framework. The experimental permeate flux, GOR and STEC were predicted using a dataset of 36 experimental runs with three inputs, namely: feed temperature (45-75°C), feed flow rate (1-3 lpm) and coolant flow rate (1-3 lpm). The RF models were highly accurate, with training R2 values of 0.978 (flux), 0.953 (GOR), and 0.904 (STEC), and the RF models were backed by good cross-validation results. Feed temperature was found in feature importance and SHAP analysis as the most influential parameter, whereas feed flow rate and energy recovery were the most influential parameters with secondary effects, and coolant flow rate was not significant. A parametric analysis also provided the interactions among operating variables. A Genetic Algorithm (GA) coupled with the RF model identified optimal conditions (Tf = 71.71°C, FFR = 1.295 lpm, CFR = 2.665 lpm), yielding Flux = 7.176 kg m⁻² h⁻¹, GOR = 3.308, and STEC = 82.88 kWh m⁻³, with substantial energy reduction. The suggested RFGA hybrid model is a practical and interpretable method of optimization of next-generation CAGMD systems.*

Keywords *- Cylindrical Air Gap Membrane Distillation, Random Forest, Machine Learning, Genetic Algorithm, Permeate flux, Feature importance, SHAP.*

1. Introduction

The surging water crisis in the world today has compelled the scientific community to seek innovative and sustainable forms of desalination in an aggressive manner to ensure access to clean drinking water. The unusual ability to work at lower pressure and use of low-grade thermal energy, including solar or industrial waste heat, has attracted a considerable amount of attention to Membrane Distillation (MD) [1], and especially to Air-Gap Membrane Distillation (AGMD) [2]. AGMD significantly minimizes conductive heat losses by placing a stagnant air layer between the hydrophobic membrane and the condensation surface, and enhances the overall performance [3]. A novel design of MD systems, Cylindrical Air Gap Membrane Distillation (CAGMD) module [4], is designed to enhance the economic feasibility and reduce the spatial footprint of such systems. This new architecture is inspired by the design of shell-and-tube heat exchangers, which are traditional, but uses a flat-sheet, hydrophobic membrane, polytetrafluoroethylene (PTFE) wrapped around a cylinder held together with a polypropylene net. In this module, hot saline feed water circulates in the annular space between the outer shell and the membrane, whereas cold fluid circulates in an innermost hollow copper tube, which serves as the condensation surface (Figure 1) [5]. One of the main strengths of the CAGMD design is the focus on cost-effectiveness and flexibility of design. In contrast to traditional AGMD systems, which focus on maximising the condensation area, this cylindrical system specially has a smaller condenser area relative to the effective membrane area, which greatly reduces manufacturing and material expenses. An air gap is created between the membrane and the central copper tube. Moreover, the cylindrical module can be configured vertically, thus becoming capable of running with a gravity feed flow [6]. All these unique geometric changes can change the internal hydrodynamics and heat transfer mechanics, so it shall be examined how the operational parameters, such as feed temperature and flow rates, affect the permeate flux of the system [7]. Literature finds that the heat and mass transfer dynamics in membrane distillation units by trial-and-error experimentation or by computationally demanding numerical techniques, including Computational Fluid Dynamics (CFD), are efficient and feasible over the traditional methods when the priority is distillate flux along with energy efficiency [8]. Although CFD and conventional mechanistic models are very

good in offering basic physical understanding of fluid flow and thermal distribution, these deterministic models tend to be based on highly simplified assumptions that make it difficult to effectively capture the dynamics of membrane operation with time [9]. This is especially in the case of complex module geometries like CAGMD to predict localised flux declines or to optimise operational parameters.

To address these barriers to analysis, Artificial Intelligence (AI) and Machine Learning (ML) are highly employed nowadays to analyse and optimize the membrane systems. In exploring Membrane Fouling Prediction Using ANNs, researchers found that AI-based models accurately learn complex patterns to forecast fouling behaviour in water treatment. For example, an ANN model successfully predicted experimental observations with less than a 5% absolute error in a full-scale Nanofiltration (NF) process, while various Multilayer Perceptron (MLP) architectures achieved incredibly high coefficients of determination, such as R^2 0.998 and R2 0.997, proving their efficacy in system optimization [10].

Chong et al.,presented a broad review on advances of machine learning in materials science that explores the transition from traditional feature engineering to representation learning and inverse design. It highlights how methodologies like decision trees, deep learning, and reinforcement learning are being increasingly adopted to bridge the gap between numerical analysis and autonomous material discovery in complex physical systems [11].

Wang et al.,studied accelerating solar-powered desalination through transferable learning, the authors analyze cost and efficiency trends over four decades using Specific Water Productivity (SWP) and Specific Energy Consumption (SEC) metrics. With the use of a de-scaled learning curve model on historical data, the research revealed learning rates of 23% for Multi-Effect Distillation (MED), 30% for Multi-Stage Flash (MSF), and 12% for Reverse Osmosis (RO), highlighting the impact of economies of scale to drive future cost reductions [12]. Ahmed et al.,utilized an Extreme Gradient Boosting (XGBoost) algorithm focusing on process optimization for experimental evaluation of a water desalination system using an optimized machine learning approach. The optimized model predicted distillate parameters with a remarkably low 1.42% Mean Squared Error (MSE) and 2.91% Root Mean Squared Error (RMSE), reducing prediction errors by 46% to identify optimum operating values of 7,580 ml/h for distillate, 53.8°C for feed heating, and 49.9°C for condensing unit temperatures [13]. Ganthavee et al., presented a study on deploying artificial intelligence and machine learning to optimize pharmaceutical wastewater treatment systems in biological treatment simulations. Data mining techniques achieved coefficients of determination greater than 0.90 when forecasting Biochemical Oxygen Demand (BOD) and Chemical Oxygen Demand (COD); additionally, hybrid models like ANN-GA and ANN-PSO reached predicted decontamination efficiencies of 89.3% and 93.5%, respectively, alongside an 87.1% lead removal efficiency [14]. To implement the Intelligence analysis of membrane distillation via machine learning models for pharmaceutical separation carried out by Alkhammash et.al, a dataset of 3,401 data points was processed using the Red Deer Algorithm. The Multi-layer Perceptron (MLP) achieved the highest accuracy with an R^2 of 0.9955, an MAE of 0.0084, and an RMSE of 0.0148, outperforming Gamma Regression (R^2 0.9214) and Support Vector Regression (R^2 0.8710) [15].

The paper Machine Learning in Membrane Design outlines how ML accelerates the screening of polymeric and 2D materials. A neural network applied to 147 polymers achieved correlation factors R^2 up to 0.999 for gas permeability, and a separate Gaussian Process Regression screened over 11,000 polymers to identify candidates surpassing the traditional upper bound. Additionally, a CatBoost model predicted nanopore formation probabilities with an R2 of 0.97 [16]. Building upon database construction, Yin et al.,utilized AI to screen 11,325 polymers against the Robeson upper bound, successfully pinpointing novel materials. For thin-film nanocomposite (TFN) membranes, optimized ANN models yielded an exceptional R2 of 0.9938 for permeate flux and 0.9811 for foulant rejection on unseen test data [17]. In another study, Ritt et al.,employed Machine learning to reveal key ion selectivity mechanisms in polymeric membranes. The transport of 18 different anions across cellulose acetate membranes was analysed. The study found a poor correlation between hydration energy and permselectivity, R^2 of 0.37 and noted that entropy-enthalpy compensation led to a free-energy barrier variation of only 8 kJ/mol, with ML revealing that electrostatic features accounted for 75% of the overall predictive features [18]. In the Study of Membranes with Nanotubes to Enhance Osmosis Desalination, Amari et al.,artificial neural networks were trained to predict water flux in reverse osmosis systems enhanced by carbon nanotubes. Using 70% of the experimental data for training, the optimized predictive model demonstrated remarkable accuracy, achieving a Coefficient of Determination R^2(R2) of 0.98 and a Mean Absolute Error (MAE) of just 1.38% [19]. Xu et.al. Synergised machine learning algorithms to study and intelligently simulate the molecular structure of the membrane and performed the experiment with a curated dataset of 152 measurements, covering 35 polymers and 16 solvents to develop Organic Solvent Nanofiltration (OSN) membranes. The resulting PIM-A1 membrane, validated by ML algorithms (KRR, GBR), experimentally exhibited a methanol permeability of 2.33×10^{-6} L·m/m²·h·bar and a near-perfect solute rejection rate of 99.87% [20]. In exploring Different mathematical models based on artificial intelligence techniques to predict solute concentration distribution, an Adaboost methodology was applied to over 8,000 data points. The Boosted K-Nearest Neighbors (KNN) model emerged as the most appropriate,

achieving an R2 of 0.9853, an MAE of 20.73, and a Mean Absolute Percentage Error (MAPE) of 1.06×10^{-2}, handily outperforming linear regression R^2 0.8751 and Gaussian Process Regression R^2 0.9793 [21]. An Interpretable deep learning approach for designing nanoporous silicon nitride (NPN) membranes successfully combined Generative Adversarial Networks (GANs) and Convolutional Neural Networks (CNNs). The framework generated custom microstructures for prescribed strength targets (0.4, 0.7, 1.0, and 1.3 GPa) and ultimately yielded an optimised design reaching 1.58 GPa at a porosity of 0.189, outperforming conventional homogenous pore patterns [22]. The review on Leveraging ML in porous media evaluates various algorithms like Support Vector Machines and Decision Trees. When applied to polybenzimidazole (PBI) membranes for vanadium redox flow batteries, the neural network models predicted voltage and energy efficiency with a Mean Absolute Prediction Error (MAPE) of less than 1% compared to experimental data [23]. In evaluating the Membrane desalination process powered by solar energy, a Stacking ensemble method combining MLP and XGBoost was applied to 45 observations. The Stacking model significantly outperformed single models, achieving an R2 of 0.99043 on the test set, with the lowest test errors recorded at an RMSE of 6.17921 and an MAE of 5.90072 [24]. In ML models, complex, non-linear correlations are learned by analysing experimental or simulated data. The Random Forest (RF) algorithm has become one of the most powerful tools in the ML environment that can be applied to membrane design and process prediction. Random Forest is an ensemble learning method that combines and sums several decision trees, which is called bootstrapping and bagging, obtaining an overall and very accurate output. Contrary to single algorithms, Random Forest is very robust to overfitting, multi-variable settings can be easily tackled, and the algorithm has shown impressive accuracy in predicting vital membrane parameters such as permeate flux and fouling propensities.

Despite the considerable advances in membrane science in recent times with data-driven methods, the use of ensemble algorithms in specifically assessing and optimizing cylindrical AGMD configurations is a mostly untapped frontier. From the literature reviewed, it is evident that machine learning has been widely used to predict membrane fouling, to screen suitable polymers and to analyze the flat-sheet or the vacuum membrane distillation configuration, with R^2 values more than 0.90. None of the literature has studied cylindrical AGMD geometry, in which the feed channel in the annulus part of the AGMD, the central condenser tube and the reduced condensation to membrane area ratio affect the heat and mass transfer characteristics differently from flat-sheet AGMD, and have not been accounted for by any optimization models. Theoretical and experimental characterization has been used in prior CAGMD studies [4], but until now, there has been no study attempting to combine an interpretable ensemble model with an evolutionary optimizer to find optimized operating conditions for this configuration. The need to fill such a gap, i.e., the lack of an interpretable and optimization-ready ML framework for CAGMD systems, is the problem that this study tries to solve. Thus, the current paper is a detailed performance evaluation of a cylindrical air gap membrane distillation system based on a Random Forest machine learning model.

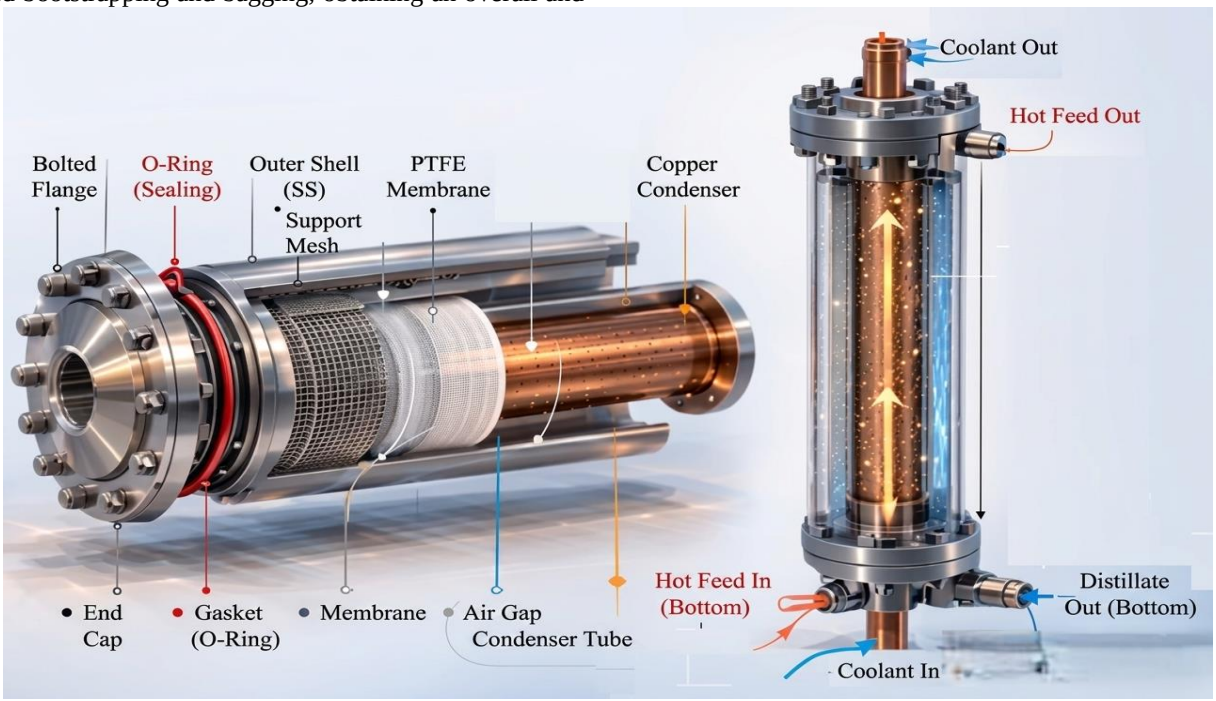

Fig. 1 Module design of the cylindrical air gap membrane distillation system

This study seeks to predict output parameters, viz., permeate flux, Gained Output Ratio (GOR) and the energy performance of the system by identifying Specific Thermal Energy Consumption (STEC) with accuracy using different conditions by training the predictive model on key operations inputs. In addition, there is no published research that has integrated RF-based interpretability (feature importance, SHAP) with a GA optimizer for the cylindrical AGMD module, unlike the other MD configurations and the flat-sheet AGMD module. Finally, the aim of this work is to offer a fast, reliable and computationally lean framework to optimize the cylindrical AGMD modules to achieve next-generation, energy-efficient water purification.

This work combines Random Forest regression with a cylindrical AGMD module, dual interpretability analysis (impurity-based feature importance and SHAP) and a Genetic Algorithm optimizer, which differ from previous machine-learning studies on membrane distillation, which focused on flat-sheet AGMD, vacuum-assisted AGMD or photothermal MD module. The combination of these three features (cylindrical geometry, dual method interpretability and RF-GA hybrid optimization) has not been reported together for any membrane distillation configuration and is the specific contribution of this paper.

To achieve the above objectives, the present study aims to: (i) Develop Random Forest regression models to model permeate flux, GOR and STEC of a cylindrical AGMD system as a function of three operating inputs (feed temperature, feed flow rate and coolant flow rate); (ii) Evaluate the relative importance of each operating parameter on each model output using impurity-based feature importance and SHAP analysis; (iii) Characterize the parametric response of the system throughout the entire experimental operating regime; and (iv) Integrate the trained RF system with a Genetic Algorithm to determine the operating conditions that maximize productivity, energy efficiency, while minimizing energy consumption.

Random Forest was chosen for this because it is more tolerant of the small, unevenly distributed experimental data than gradient-based models, is not sensitive to feature scaling and can give directly interpretable feature importance scores, which are very useful when the experimental data set has only 36 experimental runs, as in this case.

2. Materials and Methods

2.1. Materials and Experimental Setup

To test the performance of desalination under controlled conditions, a cylindrical Air Gap Membrane Distillation (CAGMD) module was used. The system comprises of a stainless steel outer shell, a hydrophobic PTFE membrane, an air gap area and a copper condenser tube, all in a concentric arrangement. Polytetrafluoroethylene (PTFE) was used as the membrane because it is very hydrophobic, chemically resistant, and thermal resistant. A support mesh was added to give mechanical strength and to avoid deformation of the membrane when subjected to operating pressures.

An annulus Copper tube was used as a condenser tube, which is highly thermal conductive, which allows easy condensation of the vapor. O-rings and bolted flanges were used to seal the system to become leakproof. Figure 2 gives the comprehensive information about the experimental system details, along with a clear overview of operating input and output parameters.

2.2. Experimentation and Flow Configuration

- Hot feed enters from the bottom and flows upward along the membrane surface.
- Water vapor passes through the membrane pores into the air gap.
- Vapor condenses on the cooled copper condenser surface.
- Coolant flows counter-currently to enhance heat transfer.
- Distillate is collected at the bottom outlet.

A total of 36 experimental samples were obtained after data preprocessing and deduplication. The dataset consists of Input parameters (3): Feed temperature (°C), Feed flow rate (L/min), and Coolant temperature (°C). whereas the Output responses (3) are Permeate flux (kg/m²·h), Gained output ratio (GOR) and Specific thermal energy consumption (STEC). The dataset was divided using an 80:20 train-test split, ensuring representative distribution across operating conditions.

3. Results and Discussion

3.1. Machine Learning Framework

A Random Forest (RF) regression model was applied to model the nonlinear relationships between process variables and performance indicators. Random Forest algorithm was chosen because it is very resistant to overfitting, capable of capturing nonlinear interactions, as well as high interpretability as a result of feature importance.

In contrast to gradient-based algorithms like neural networks or support vector regression, RF is also feature-scaling invariant, meaning that it was not necessary to normalise the input or output variables with a view to scaling them. The data was randomly divided into a training subset (n = 28) and a test subset (n = 8) in a stratified random split with a fixed seed to reproduce the study.

The GridSearchCV did the hyperparameter tuning and experiments with the combinations listed in Table 1. Each of the output variables was searched independently, such that the model was optimized independently to each response. The optimized parameters were Number of trees (n_estimators), Maximum depth (max_depth) and Minimum samples split and leaf nodes.

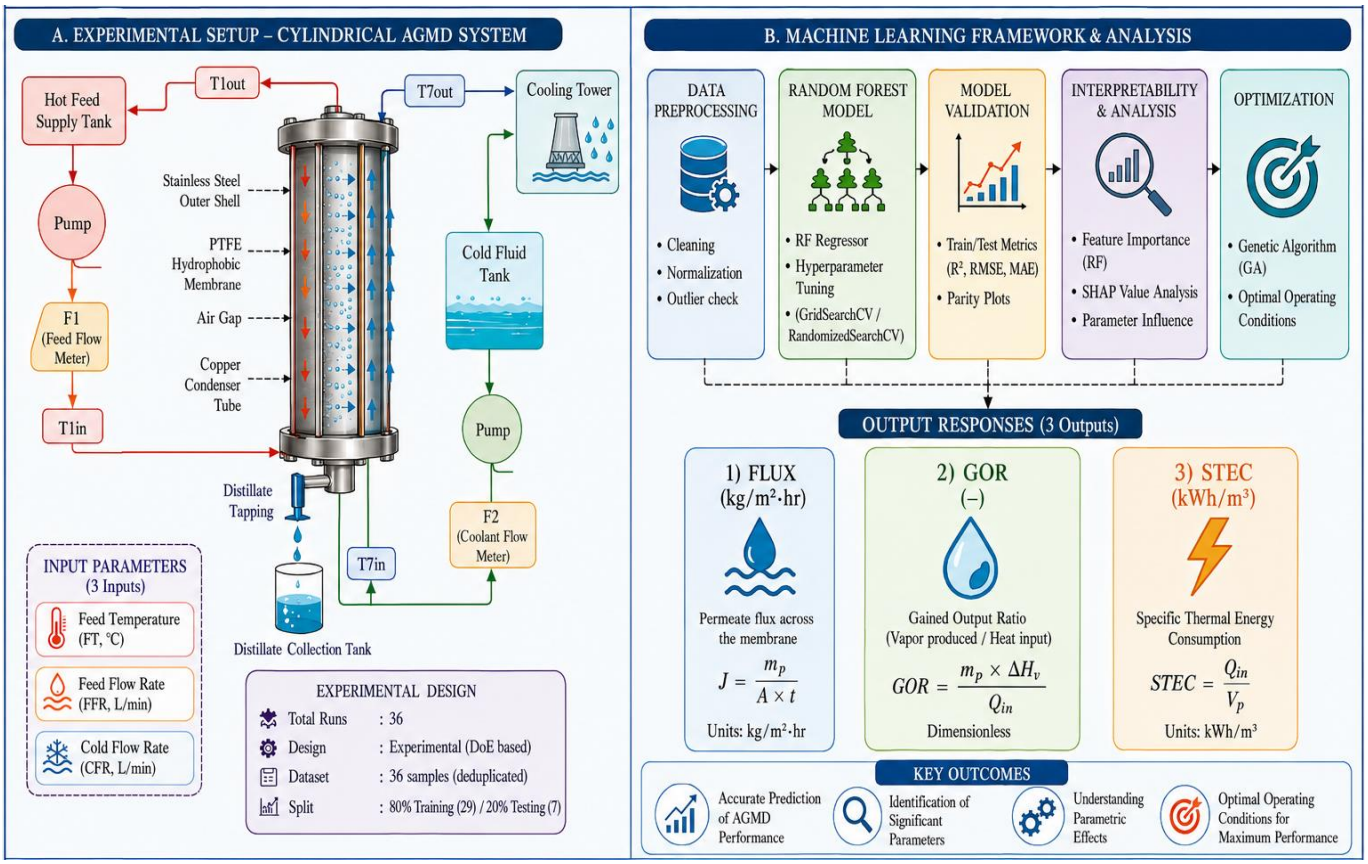

Fig. 2 Methodology and experimental setup details for the CAGMD system

Table 1. Hyperparameter search space used in GridSearchCV

Hyperparameter	Values explored	Header Selected (Flux / GOR / STEC)
n_estimators	{100, 200, 300}	100 / 100 / 100
max_depth	{None, 5, 10, 15}	None / None / 5
max_features	{sqrt, log2, 0.8}	sqrt / sqrt / sqrt
min_samples_split	{2, 4, 6}	2 / 2 / 2
min_samples_leaf	{1, 2, 3}	1 / 1 / 1

The selected hyperparameters are shown in the final column of Table 1. The flux and GOR models both favoured unconstrained tree depth, indicating that deeper splits capture real structure in these responses rather than noise. The STEC model settled on max_depth = 5, which makes physical sense: STEC spans a much wider absolute range than the other two outputs. In all three cases, with minimum samples split and leaf nodes, the feature-selection fraction of sqrt and 100 trees was sufficient, suggesting the response landscape is smooth enough that a moderately sized forest captures it well.

3.2. Model Validation and Performance Metrics

Model accuracy was assessed using four metrics: R^2, Root Mean Square Error (RMSE), mean absolute error (MAE), and Mean Absolute Percentage Error (MAPE). These were calculated separately on the training and test sets. A ten-fold cross-validation (10-CV) was also performed on the full dataset to give a more stable generalisation estimate than the single 80:20 split alone. All metrics are collected in Table 2, and the parity plots are shown in Figure 3.

Table 2. RF model performance metrics for all three output variables

Output	R^2 (train)	R^2 (test)	RMSE (train)	RMSE (test)	MAE (test)	MAPE (test)
Flux	0.978	0.736	0.329	0.773	0.684	21.4%
GOR	0.953	0.675	0.135	0.656	0.520	38.8%
STEC	0.904	0.669	60.61	148.54	100.91	43.6%

Table 2 shows that the training R^2 values of Flux, GOR and STEC being positive represent the highly accurate model development for prediction. As the test set, the scores fall to 0.736, 0.675, and 0.669, respectively, a difference that is large in relative terms but needs to be read attentively at this sample size. The test R2 can shift by 0.05-0.10 with a one standard deviation error in a single prediction that is an outlier. The more honest summary of the model generalisation is the ten-fold cross-validation that sequentially cycles through each of the 36 points in the test role: 0.741 in flux, 0.676 in GOR, and 0.561 in STEC. These results are in line with those that RF models obtain on the same-sized systematic MD datasets in the literature [25-28].To visually understand the model accuracy, parity plots were generated for all output variables.

Figure 3 parity plots show and compare the predicted values to experimental values of the training and test data. The points are near the 45° reference line over the entire operating range of all three outputs, and there is no apparent trend of systematic over- or under-prediction in any one region. STEC shows the largest absolute errors, which is not unexpected.

STEC is defined as the ratio of thermal energy consumed to permeate volume produced [29-31], so prediction errors in flux are amplified when flux is low, specifically at the high FFR, low FT, low CFR regions of the operating space where vapour production is limited. This error amplification at low-productivity conditions explains the higher MAPE of 43.6% for STEC relative to 21.4% for flux, even though the underlying R^2 values are similar.

3.3. Feature Importance and Interpretability Analysis

Understanding which operating variable affects each output most strongly helps to identify the areas where the focus should be done to control effort. The influence of variables was ranked in two ways: the built-in Random Forest feature importance and Shapley Additive Explanations (SHAP). The Random Forest feature importance is a measure of the average variance reduced by each variable on the nodes where the variable is used to split, on average across all the trees. SHAP values are a complement: they determine, on a per-prediction basis, local and global interpretability, quantitative contribution of each input variable and insight into parameter sensitivity, the marginal contribution of each variable over the average prediction [27].

The two approaches are in agreement with each other in this area, and this serves as a booster of the ranking that the rankings represent the actual physics. All the importance scores are summarised in Table 3. Feed Temperature (FT) is the dominant variable for permeate flux, accounting for 73.1% of the RF importance and producing a mean SHAP magnitude of 1.667 kg m^{-2} h^{-1}, more than three times the combined contribution of FFR and CFR. This result is explained by the governing transport physics. Vapour pressure follows an exponential relationship with temperature (Antoine equation), so raising FT from 45 °C to 75 °C does not linearly double the driving force; it roughly quadruples it. The experimental data reflect this: at FFR = 2 lpm and CFR = 2 lpm, increasing FT from 45 to 75 °C raises flux from 3.21 to 7.12 kg m^{-2} h^{-1}, a factor of 2.2 over a 30 °C span.

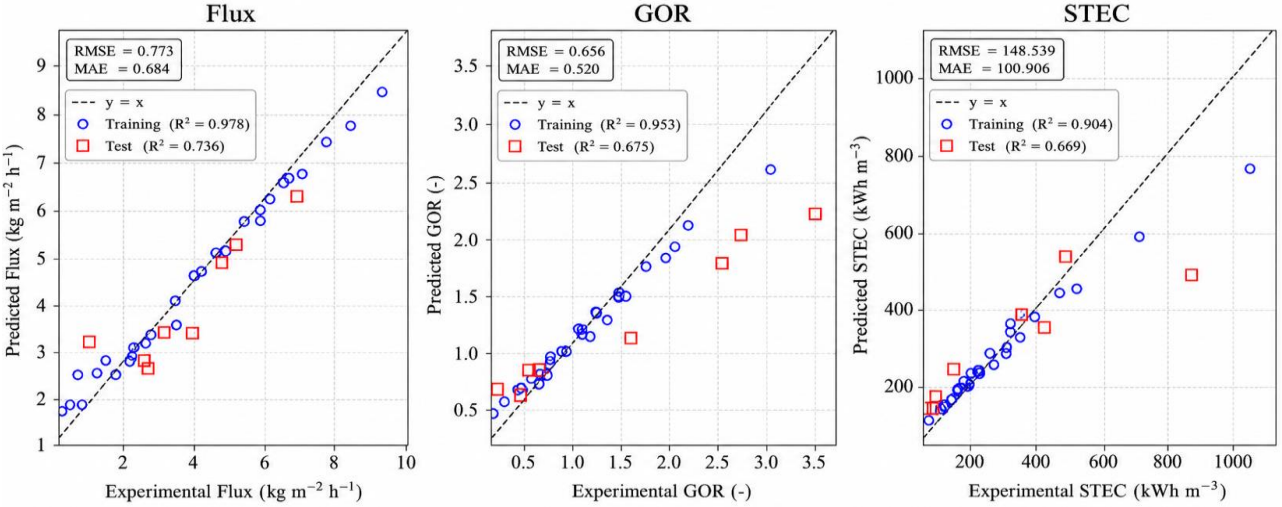

Fig. 3 Parity plots for the random forest machine learned CAGMD model

Table 3. RF impurity-based importance and mean |SHAP| values for each input variable

Output Parameter	Input Parameter	RF Importance (%)	Mean |SHAP|	Rank
Flux	FT	73.1	1.667	1st
Flux	FFR	17.6	0.542	2nd
Flux	CFR	9.2	0.330	3rd
GOR	FT	63.8	0.391	1st

GOR	FFR	26.4	0.208	2nd
GOR	CFR	9.7	0.090	3rd
STEC	FT	63.3	101.7	1st
STEC	FFR	23.6	55.3	2nd
STEC	CFR	13.2	27.7	3rd

CFR comes second in terms of flux (9.2% importance, SHAP = 0.330), followed by FFR (17.6% importance, SHAP = 0.542). The importance inversion here is FFR above CFR, SHAP between them. This is interpreted that FFR influences more split nodes in the trees because it varies continuously, but the contribution of CFR and FFR to flux per-prediction is similar. In the range of CFR 1–3 lpm investigated, at constant FT = 65 C and FFR = 2 lpm, flux increases with change of CFR 1 to 3 lpm by 32 per cent - significant, but less than the 54% increase with change in FT with constant FFR [28].

In the case of GOR, FT contributes the largest share (63.8%), whereas FFR contributes a higher share relative to flux (26.4%). At a reduced FFR, the feed will spend a longer time in the module, and internal heat exchange between the condensate in the gap and the feed channel is more complete. At FT = 65 °C and CFR = 2 lpm, reducing FFR from 3 to 1 lpm raises GOR from 0.953 to 2.232, a 134% increase. This is a more powerful sensitivity than can be had by varying CFR at the same conditions, where the GOR range is 0.839-1.314, with a spread of 57%.

In the case of a high FT, a high flux and a high fixed thermal input distributed over a greater volume of permeate, the energy cost per litre produced is reduced. The lowest STEC observed in the dataset was 74.6 kWh /m3 at FT = 75 °C, FFR = 1 lpm, CFR = 3 lpm and the highest was 1034.9 kWh /m3 at FT = 45 °C, FFR = 3 lpm, CFR = 1 lpm. The high folds span of the operating range highlights the sensitivity of operating conditions to energy performance in CAGMD. The absolute values of SHAP of STEC (FT: 101.7, FFR: 55.3, CFR: 27.7 kWh /m3) are a result of the large absolute range of STEC.

The combined analysis of the importance reveals three observations. To begin with, FT is the major contributor of both the productivity measures (flux, STEC), whereas FFR is the major driver of the energy efficiency measure (GOR). This implies that high productivity and high efficiency are anti-optimal with FT on the control, but more optimal with FFR on the control. Decreasing FFR increases GOR and does not heavily punish flux (the flux sensitivity to FFR is 17.6%, which is much lower than its flux sensitivity to FT). Second, CFR is consistently ranked in the third place in all three outputs and both attribution approaches, yet its contribution is not insignificant, 913% importance, and it cannot be arbitrarily fixed without impacting the performance of systems. Third, the three variables are not redundant and each of them has some meaningful information to at least one of the outputs. This verifies that all three are essential to optimisation of this system and that a one-variable control problem would not capture cross-variable interactions that call for multi-objective optimisation for the balanced system performance determination.

3.4. Parametric Analysis

A systematic parametric study was conducted using the trained RF model to evaluate the effect of individual input variables on system performance. Each parameter was varied within its experimental range while keeping other variables constant, enabling Sensitivity analysis, identification of optimal operating regions and understanding of system behaviour trends. The discussion on the parametric analysis is represented by considering the model output in comparison with the experimental outputs to simultaneously understand the correlation between them. The explanations are given with the help of 2D charts as well as with the surface plots to enable multi-parametric study on the output.

3.4.1. Effect of Feed temperature on Output parameters

The Figure 4(a), and (b) present the parametric response of the CAGMD system to variations in feed temperature (Tf) across the experimental range of 45–75 °C, with the Coolant Flow Rate (CFR) fixed at 2 lpm and the Feed Flow Rate (FFR) varied at three discrete levels Black markers in each figure represent the measured experimental data points, while the continuous lines denote the RF model predictions interpolated within the operating space. The figure shows that there is a very strong and steady nonlinear increase in the permeate flux with the increase in the feed temperature at all three levels of FFR. At FFR = 2 lpm and CFR = 2 lpm, the experimentally measured flux increases from 3.21 $kg.m^{-2}.h^{-1}$ at Tf = 45 °C to 7.12 $kg.m^{-2}.h^{-1}$ at 75 °C, representing a 121.8% enhancement over a 30 °C span.

This is regulated by the exponential dependence of saturated vapour pressure on temperature, as defined by the Antoine equation: a slight increase in feed temperature exponentially raises the transmembrane vapour pressure gradient, which forms the main force behind mass transfer across the hydrophobic PTFE membrane.

This nonlinear profile is well represented by an RF model that predicts well within an experimental range of all FFR conditions (training R2 = 0.978). It is interesting to note that the influence of FFR on flux is relatively weak; the three FFR curves are well spaced across the range of temperature, which is in line with the low RF feature significance of FFR on flux (6.3%).

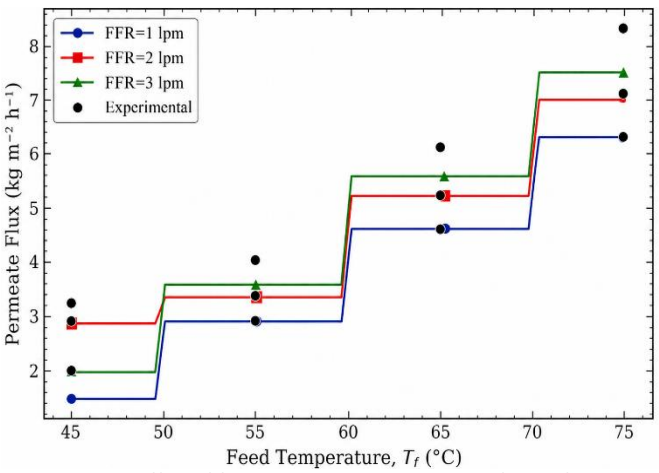

Fig. 4(a) Effect of feed temperature on permeate flux at fixed CFR=2lpm

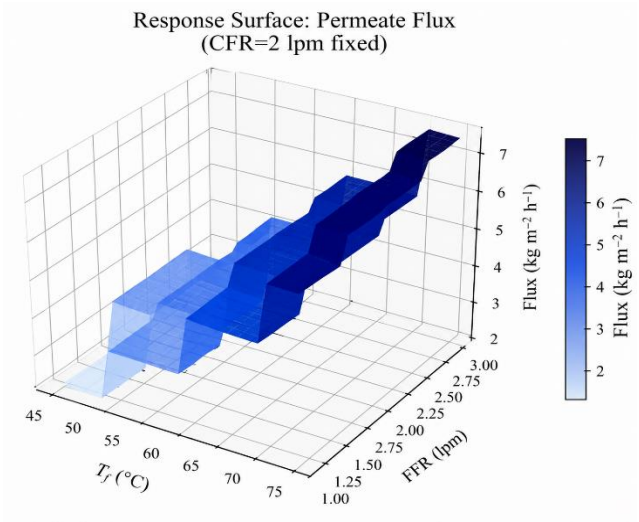

Fig. 4(b) Surface plot to show the effect of Feed temperature on permeate flux at fixed CFR=2lpm.

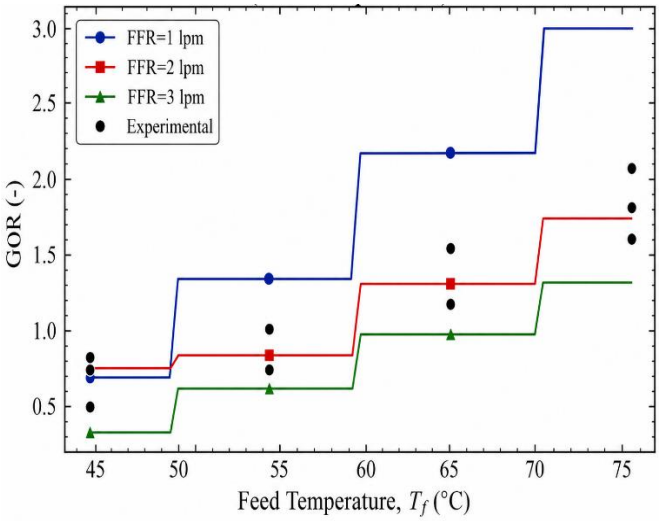

Fig. 5(a) Effect of feed temperature on Gained Output Ratio (GOR) at CFR = 2lpm

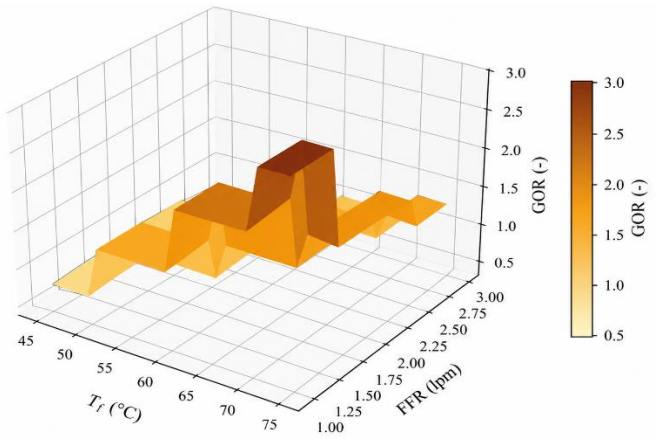

Fig. 5(b) Surface plot to show the effect of feed temperature on Gained Output Ratio (GOR) at CFR = 2 lpm.

Experimentally, a maximum flux of 9.08 kg.m^{-2}.h^{-1} was obtained at FFR = 3 lpm and CFR = 3 lpm at 75 °C, which confirms that the dominant driving force in the control of CAGMD productivity is the thermal driving force.

Figure 5 (a), and (b) shows how the feed temperature affects the Gained Output Ratio (GOR). There is a monotonic increase in GOR with temperature at all levels of FFR; at FFR = 2 lpm and CFR = 2 lpm, the increase in GOR is 0.80 at 45°C, to 1.80 at 75°C, or about 125%. The physical mechanism behind this trend is that as temperature increases, the rate of permeate production increases. This tendency is reflected in the RF model that has a training R2 equal to 0.953 in the case of GOR. A key finding is the sharp separation of the FFR curves at higher temperatures: at Tf = 75°C, GOR = 3.08 at FFR = 1 lpm compared to GOR = 1.31 at FFR = 3 lpm, indicating the synergistic nature of high temperature and low flow rate in promoting energy recovery, which is supported by the RF feature importance of 35.9% attributed to FFR.

Figure 6 (a), and (b) shows the Specific Thermal Energy Consumption (STEC, kWh.m -3) change with feed temperature at CFR = 2 lpm. STEC shows a decline with rising Tf, which shows the enhancement of thermal efficiency at higher operating temperature. At FFR = 2 lpm, STEC declines from 324.9 kWh m^{-3} at 45 °C to 146.5 kWh m^{-3} at 75 °C, a reduction of approximately 54.9%. STEC is negatively proportional to permeate flux, physically because flux rises exponentially with temperature, as fixed thermal input to the feed is relatively constant, the energy price per unit volume of distillate drops exponentially. The separation of the FFR curves is most evident at low temperatures, with lowered vapour generation at high FFR leading to an extreme penalty at STEC: the highest experimental values of 1034.9 kWh m -1, Tf = 45°C, FFR = 3 lpm, CFR = 1 lpm were obtained. RF model (training R 2 = 0.904, test R 2 = 0.669) captures the overall downward trend and curve-separation behavior, and the prediction accuracy increases with higher temperatures,

where the flux is less susceptible to small measurement errors. The importance of RF impurities (61.4) and the average value of SHAP (101.7 kWh m -3) confirmed feed temperature as the main force of STEC, highlighting the essential role of thermal control in the CAGMD process.

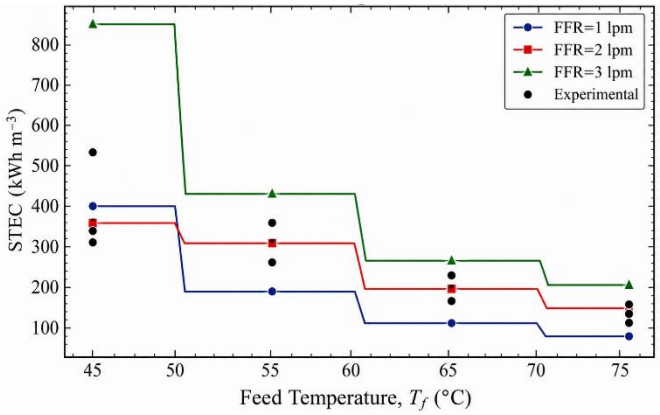

Fig. 6(a) Effect of feed temperature on Specific Thermal Energy Consumption (STEC) at CFR = 2 lpm

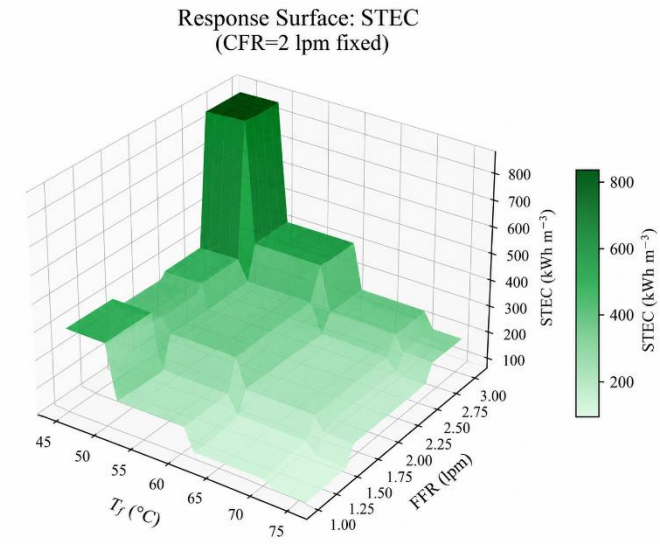

Fig. 6(b) Surface plot to show the effect of feed temperature on Specific Thermal Energy Consumption (STEC) at CFR = 2 lpm.

3.4.2. Effect of Feed Flow Rate (FFR) on System Performance

Figure 7 illustrates the response of permeate flux variation with feed flow rate at the feed temperatures at a constant CFR of 2 lpm. In contrast to the traditional MD systems, in which the increased flow rates always lead to the increased flux due to the better mixing in the boundary layers, there is a mild, non-monotonic sensitivity of the CAGMD module. At Tf = 65 °C, flux increases modestly from 4.43 kg m^{-2} h^{-1} at FFR = 1 lpm to 5.66 kg m^{-2} h^{-1} at FFR = 3 lpm, a rise of only 27.8%. At Tf = 75 °C, the increase from FFR = 1 lpm (6.09 kg m^{-2} h^{-1}) to FFR = 3 lpm (7.72 kg m^{-2} h^{-1}) is similarly subdued at approximately 26.8%. This low sensitivity is due to the fact that the CAGMD module with its cylindrical annular geometry ensures a relatively thin thermal boundary layer at low flow rates, such that even the small increase in convective heat transfer at the higher FFR do not change the vapour pressure gradient significantly. These small trends are accurately captured by the RF model (training R2 = 0.978), and the low feature importance of FFR to flux (6.3 percent) is also consistent with the narrow distribution of the flux curves at each flow rate at a fixed temperature.

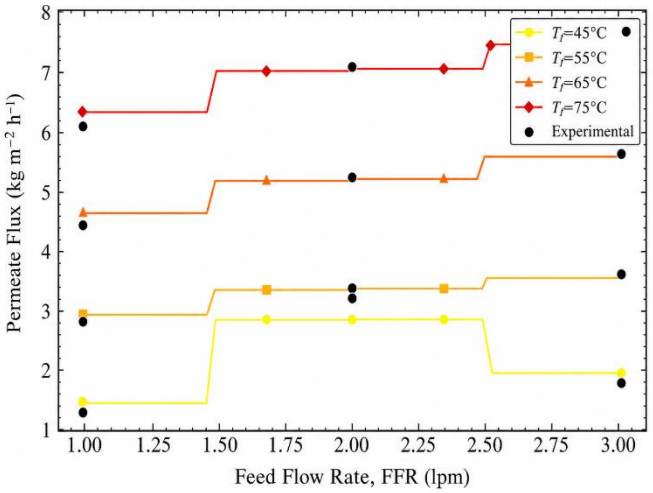

Fig. 7 Effect of feed flow rate on permeate flux at CFR = 2 lpm

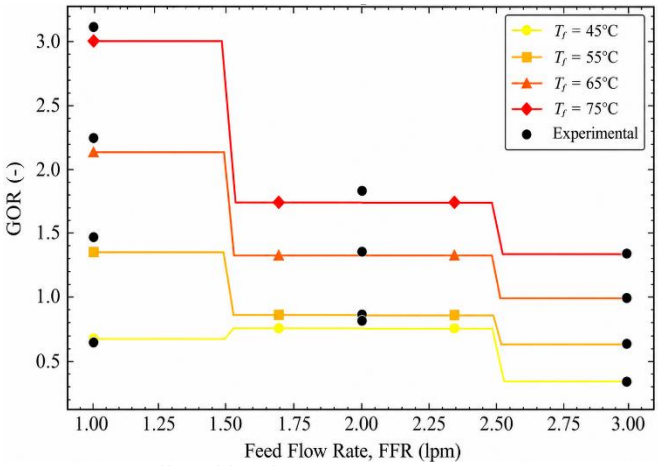

Fig. 8 Effect of feed flow rate on GOR at CFR = 2 lpm

The sharpest parametric sensitivity can be seen in Figure 8, where GOR decreases progressively and consistently with an increment in FFR and the impact is enhanced significantly with the increment of feed temperature. At Tf = 75 °C and CFR = 2 lpm, the experimentally measured GOR falls from 3.08 at FFR = 1 lpm to 1.31 at FFR = 3 lpm, a decline of 57.5%. The reduction at Tf = 65 C is between 2.23 and 0.95, which is a reduction of 57.4. The principle behind this is internal heat recovery; at lower FFR, the feed has a longer residence time in the module, allowing the incoming feed stream to more thoroughly exchange heat with the condensate in the air gap. The shorter contact time decreases the

usefulness of this internal recuperation as the FFR increases, resulting in an increased amount of unused thermal energy leaving the system, hence reducing the GOR.

This behaviour highlights the fact that GOR is essentially a residence-time-based efficiency measure, as opposed to a flux-based measure. The RF model shows that FFR has the largest |SHAP| value in all the inputs of GOR (mean |SHAP| = 0.208), and the importance of RF features of GOR is 35.9%, which validates that FFR is the dominant control lever in the CAGMD system in energy recovery optimization.

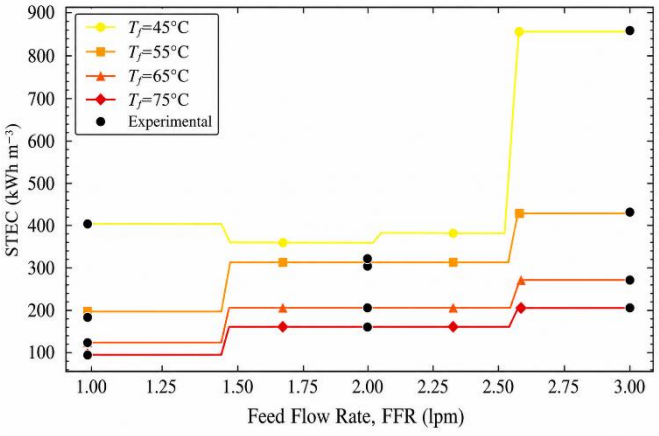

Fig. 9 Effect of feed flow rate on GOR at CFR = 2 lpm

Figure 9 shows that there exists a very strong positive correlation between feed flow rate and specific thermal energy consumption at all feed temperatures. STEC increases more than twice with increases in FFR at Tf = 65°C and CFR = 2 lpm.

This extreme STEC increase at high FFR is extremely high at low temperature: at Tf = 45°C, STEC = 873.5 kWh m -3 at FFR = 3 lpm vs. 398.2 kWh m -3 at FFR = 1 lpm. Energy balance depicts that the increased FFR needs more thermal energy to heat the increased feed volume to the operating temperature.

The gain in flux with increased FFR is relatively small (see Figure 7), so the denominator (distillate volume) increases much more slowly than the numerator (thermal input), causing the STEC to rise sharply. This trend is well represented by the RF model (training R2 = 0.904) with the impurity-based importance analysis explaining 33.5% of the variance of STEC.

3.4.3. Effect of Coolant Flow Rate (CFR) on System Performance

Figures in the discussion below illustrate the parametric response of the CAGMD system to the Cold Flow Rate (CFR) with FFR constant (2 lpm). RF model has been found to have CFR as the third most influential feature (flux: 6.9%, GOR: 4.2%, STEC: 5.1%).

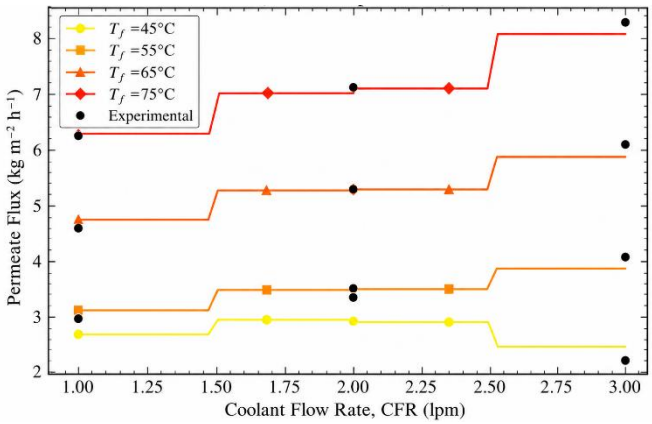

Fig. 10 Effect of coolant flow rate on permeate flux at FFR = 2 lpm

Figure 10 shows that there is a steady positive influence of the coolant flow rate on permeate flux at all feed temperatures in the CAGMD system. At Tf = 65 °C and FFR = 2 lpm, experimentally measured flux increases from 4.61 kg m^{-2} h^{-1} at CFR = 1 lpm to 6.09 kg m^{-2} h^{-1} at CFR = 3 lpm, representing a 32.1% gain. At Tf = 75 °C, the increase is from 6.33 to 8.30 kg m^{-2} h^{-1}, a 31.1% enhancement. This behaviour is regulated by the physical process of keeping the temperature of the condensation surface low: an increase in the coolant flow rate through the inner copper tube is more effective in removing the latent heat of the condensation interface, inhibiting the increase in the temperature of the condenser wall and hence maintaining a larger vapour pressure difference across the air gap. This directly increases the driving force of the mass transfer but does not increase the energy input to the feed. The RF model is successful in modelling the positive trend with the established positive relationship between high vapour flux and condensation capacity requirements. The corresponding small absolute significance of CFR (6.9%) relative to T - (86.8) is due to the fact that the condensation surface temperature is only able to affect the vapour pressure gradient across the air gap, but not the vapour pressure at the membrane surface itself, which is determined by the feed temperature. Figure 11 shows a surface plot of GOR versus the rate of coolant flow, showing a moderate rise but constant with all the feed temperatures. At Tf = 65 °C and FFR = 2 lpm, GOR rises from 1.16 at CFR = 1 lpm to 1.54 at CFR = 3 lpm, a 32.8% improvement. At Tf = 75 °C, the corresponding increase from 1.60 to 2.10 represents a 31.3% gain. The effect of CFR on GOR has a mechanistically different positive impact compared to FFR. Whereas the influence of FFR on GOR is largely through the manipulation of feed residence time and internal recuperation, CFR can greatly improve GOR by increasing the quality of condensation: at higher CFR, the condenser temperature is low, and thus more of the vapour-liquid conversion occurs. The RF model indicates that CFR has a feature score of 4.2% to predict GOR, and the experimental results reveal that GOR curves are closely clustered in CFR values relative to the large

separation between curves in FFR levels (Figure 8), indicating that CFR is a secondary tuning parameter to energy efficiency. However, low levels of feed temperature (T = 45 °C) show that even with all levels of CFR, GOR values do not rise above 0.9, highlighting the importance of coolant management in the absence of adequate thermal driving force.

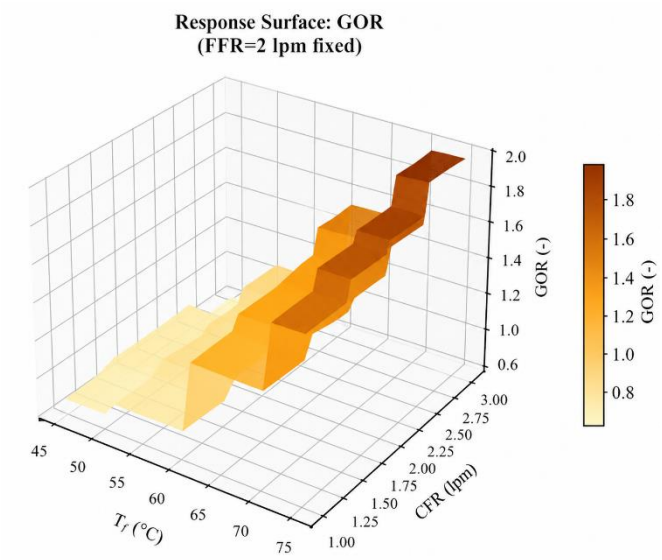

Fig. 11 Effect of coolant flow rate on GOR at FFR = 2

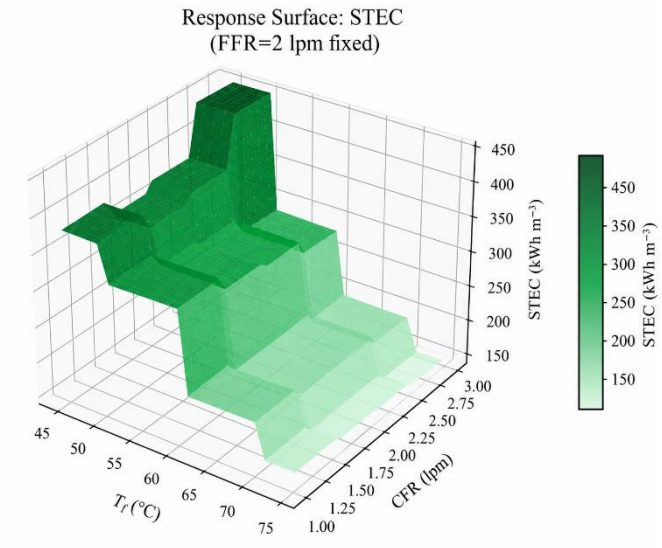

Fig. 12 Effect of coolant flow rate on STEC at FFR = 2 lpm

Figure 12 presents the surface plot of particular thermal power consumption to changes in the rate of coolant flow, and the reaction is constantly decreasing monotonically with all the considered Tf levels. At Tf = 65 °C and FFR = 2 lpm, STEC decreases from 226.6 kWh m^{-3} at CFR = 1 lpm to 171.3 kWh m^{-3} at CFR = 3 lpm, a 24.4% reduction. The respective enhancement at Tf 75°C is between 165.0 and 125.7 kWh m-1, which indicates a reduction of 23.8%. The principle is simple: an increase in CFR maintains a colder condensation surface, resulting in an increase in the vapour flux across the membrane and the rate of distillate production. The better yield of distillate directly decreases STEC since the thermal energy fed to the feed per unit time is relatively constant at a given feed temperature and FFR.

4. Genetic Algorithm Optimization

In order to determine the globally optimal CAGMD operating conditions, a Genetic Algorithm (GA) was combined with the trained Random Forest (RF) model in a hybrid RF-GA optimization model. The GA appraises every candidate solution, a combination of feed temperature (Tf), Feed Flow Rate (FFR) and Coolant Flow Rate (CFR), by consulting the RF model. The range of the search space in three dimensions was limited by experimentally validated quantities: Tf [45, 75] °C, FFR [1, 3] lpm, and CFR [1, 3] lpm. As the CAGMD system has performance objectives that are incompletely compatible (permeate flux and GOR should be maximized, and STEC should be minimized), a weighted composite fitness was created as:

$$F = (0.40 * Fluxnorm) + (0.40 * GORnorm) + (0.20 * (1 - STECnorm)) \quad (1)$$

Where each term is min-max normalized to [0, 1] using the experimental dataset bounds: Flux ∈ [1.107, 9.081] kg m^{-2} h^{-1}, GOR ∈ [0.253, 3.530], and STEC ∈ [74.62, 1034.90] kWh m^{-3}. Flux and GOR, which are the main metrics of productivity, were each weighted equally (0.40), and STEC was weighted with a 0.20. The GA was set to have a population of 30 real-valued individuals, where tournament selection (k = 4), arithmetic blend crossover (rate = 0.80) and uniform random reset mutation (rate = 0.15 per gene) were used. The complete summary of the parameters for GA is given in Table 4. To be as reproducible as possible, the random seed was set to 99.

Table 4. Summary of Genetic Algorithm configuration parameters

GA Parameter	Value	Role
Population size	30	Sufficient diversity for 3-variable space
Generations	50	Convergence plateau reached at Gen. 25
Selection	Tournament (k=4)	Moderate selection pressure avoids stagnation
Crossover type/rate	Arithmetic / 0.80	Offspring within the convex hull of parents
Mutation type/rate	Uniform reset / 0.15	Maintains diversity; prevents local optima
Objective function weights	0.40 / 0.40 / 0.20	Flux / GOR (primary); STEC (secondary)

Figure 13 shows the convergence history of the GA. The population initialized with a mean fitness of 0.413 at generation 1, reflecting the wide spread of randomly distributed candidates. Rapid improvement occurred during the first 10 generations as tournament selection consistently promoted high-Tf, low-FFR individuals, and by generation 11, the best fitness surpassed 0.80. The algorithm reached its final converged value of F = 0.876 at approximately generation 25, after which both the best and mean fitness curves plateaued with a gap of less than 0.05, confirming stable convergence. Population diversity, measured as the mean standard deviation of decision variable values, decreased from 3.24 at generation 1 to 1.09 at generation 50, which shows progressive concentration around the optimal region without full genetic drift.

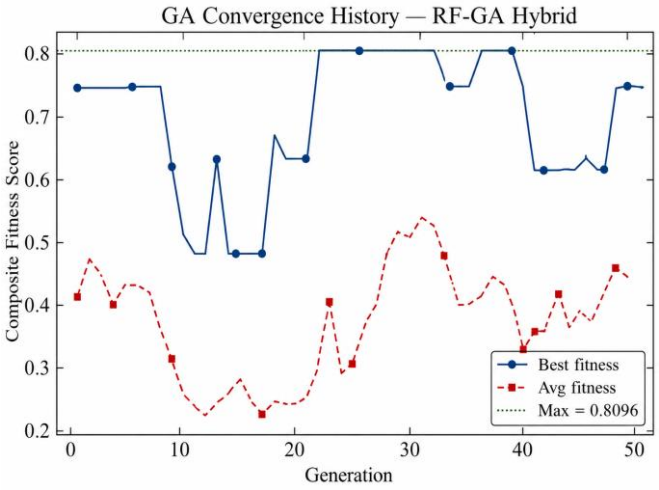

Fig. 13 GA convergence history over 50 generations

The GA identified the optimal operating condition as Tf = 71.71 °C, FFR = 1.295 lpm, and CFR = 2.665 lpm, yielding outputs of Flux = 7.176 kg m^{-2} h^{-1}, GOR = 3.308, and STEC = 82.88 kWh m^{-3}, as illustrated in Figure 14. These findings are physically consistent with the parametric trends determined in this study. Tf lies about 3 °C below the upper limit, where the marginal flux gain of further temperature rise is no longer justified by the thermal energy cost in the weighted objective; FFR is maintained nearthe lower limit to maximise GOR; and C The normalised fitness sub-scores Flux 0.664, GOR 0.867, (1-STEC 0.985) indicate that the GA solution has a near-minimum energy consumption and, at the same time, high productivity and good energy recovery (Table 5).

5. Conclusion

This paper proved the usefulness of a Random Forest machine learning model to the characterization and optimization of the performance of a Cylindrical Air Gap Membrane Distillation (CAGMD) system. RF models that were trained on 36 experimental measurements using three inputs (Tf, FFR, CFR) and three outputs (permeate flux, GOR, STEC) showed high training fidelity (R2 = 0.904) and good generalization (10-CV R2: 0.741 flux, 0.676 GOR), confirming their applicability as rapid substitutes for a physically complex, nonlinear system with limited experimental data.

Some limitations of this study are noted when interpreting the results. The models were trained using a relatively small number of experimental runs (n = 36), resulting in moderate statistical confidence of the test-set as well as the cross-validation metrics, especially for the STEC model; the R^2 for the ten-fold cross-validation (0.561) was much lower than the R^2 for training (0.904). The generalization of the trained model to other module dimensions, different membrane materials, and different feed compositions (e.g., real seawater, rather than the feed used in the present experiments) is not tested. Considering the above limitations, the next step involving this work is to attempt to address them by increasing the size of the experimental data set, comparing the model's performance with that of alternative regression methods.

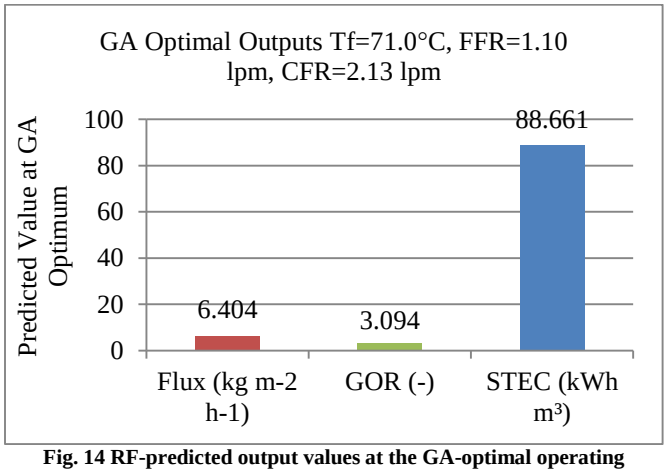

Fig. 14 RF-predicted output values at the GA-optimal operating condition (Tf = 71.71°C, FFR = 1.295 lpm, CFR = 2.665 lpm)

Overall, this research paper has validated and interpretable and optimization ready machine learning framework of the CAGMD desalination system. The optimal operating condition identified (Tf = 71.71 -1 C, FFR = 1.295 lpm, CFR = 2.665 lpm) can be directly translated into experimental validation and scale-up. The future research should aim to increase the dataset by means of active learning and adding membrane ageing and fouling effects as a further input, and confirming the GA-optimal prediction experimentally to close the gap between optimization using surrogate and physical implementation.

Table 5. GA-optimal conditions versus experimental reference points. Best experimental point: Tf = 75°C, FFR = 1 lpm, CFR = 3 lpm

Parameter	GA Optimal	Best Exp. Point	Dataset Min.	Dataset Max.
Tf (°C)	71.71	75	45	75

FFR (lpm)	1.295	1.0	1.0	3.0
CFR (lpm)	2.665	3.0	1.0	3.0
Flux	7.176	6.993	1.107	9.081
GOR (–)	3.308	3.530	0.253	3.530
STEC	82.88	74.62	74.62	1034.9
Fitness F	0.876	—	0.020	—

Conflicts of Interest

The author(s) declare(s) that there is no conflict of interest regarding the publication of this paper.

Data and Transparency Statement

No human or animal subject data were used in this study, and there was no ethical approval needed, as all the data used in this study were obtained from laboratory-scale experiments involving a non-hazardous saline feed solution. The experimental results (36 runs) and trained RF model output described in this paper are available from the corresponding author upon reasonable request. The results of the RF hyperparameter search space, GA configuration and fitness function are fully reported in Tables 1 and 4, so that the results can also be reproduced independently.

References

[1] A.M. Alklaibi, and Noam Lior, "Membrane-Distillation Desalination: Status and Potential," *Desalination*, vol. 171, no. 2, pp. 113-131, 2005. [CrossRef] [Google Scholar] [Publisher Link]

[2] Y. Elhenawy et al., "Experimental Investigation Of Two Novel Arrangements of Air Gap Membrane Distillation Module with Heat Recovery," *Energy Reports*, vol. 8, pp. 8563-8573, 2022. [CrossRef] [Google Scholar] [Publisher Link]

[3] A.M. Alklaibi, and Noam Lior, "Transport Analysis of Air-Gap Membrane Distillation," *Journal of Membrane Science*, vol. 255, no. 1-2, pp. 239-253, 2005. [CrossRef] [Google Scholar] [Publisher Link]

[4] Vandita T. Shahu, and S. B. Thombre, "Analysis and Optimization of a New Cylindrical Air Gap Membrane Distillation System," *Water Supply*, vol. 20, no. 1, pp. 361-371, 2020. [CrossRef] [Google Scholar] [Publisher Link]

[5] Vandita Thantharate Shahu, and Shashikant B. Thombre, "Theoretical and Experimental Investigation of Cylindrical Air Gap Membrane Distillation System and Effect of the Membrane Support Net on its Performance," *Environmental Science and Pollution Research*, vol. 31, pp. 7775-7792, 2024. [CrossRef] [Google Scholar] [Publisher Link]

[6] Baek-Gyu Im et al., "Theoretical Modeling and Simulation of AGMD and LGMD Desalination Processes Using a Composite Membrane," *Journal of Membrane Science*, vol. 565, pp. 14-24, 2018. [CrossRef] [Google Scholar] [Publisher Link]

[7] Hongxin Geng et al., "Study on the Heat and Mass Transfer in AGMD Module with Latent Heat Recovery," *Desalination and Water Treatment*, vol. 57, no. 33, pp. 15276-15284, 2016. [CrossRef] [Google Scholar] [Publisher Link]

[8] M. Rahimi et al., "CFD and Experimental Studies of Fouling of a Microfiltration Membrane," *Chemical Engineering and Processing: Process Intensification*, vol. 48, no. 9, pp. 1405-1413, 2009. [CrossRef] [Google Scholar] [Publisher Link]

[9] Afshin Pak et al., "CFD Modeling of Porous Membranes," *Desalination*, vol. 222, no. 1-3, pp. 482-488, 2008. [CrossRef] [Google Scholar] [Publisher Link]

[10] Waad H. Abuwatfa et al., "A Review on Membrane Fouling Prediction Using Artificial Neural Networks (ANNs)," *Membranes*, vol. 13, no. 7, pp. 1-29, 2023. [CrossRef] [Google Scholar] [Publisher Link]

[11] Sue Sin Chong et al., "Advances of Machine Learning in Materials Science: Ideas and Techniques," *Frontiers of Physics*, vol. 19, no. 1, pp. 1-40, 2024. [CrossRef] [Google Scholar] [Publisher Link]

[12] Ruoqing Wang, and Wei He, "Accelerating Solar-Powered Desalination Deployment Through Transferable Learning," *Communications Materials*, vol. 5, pp. 1-14, 2024. [CrossRef] [Google Scholar] [Publisher Link]

[13] Faizan Ahmed et al., "An Experimental Evaluation, Performance Analysis, and Improvement of Water Desalination System using Optimized Machine Learning," *Process Integration and Optimization for Sustainability*, vol. 10, pp. 737-752, 2025. [CrossRef] [Google Scholar] [Publisher Link]

[14] Voravich Ganthavee, and Antoine Prandota Trzcinski, "Artificial Intelligence and Machine Learning for the Optimization of Pharmaceutical Wastewater Treatment Systems: A Review," *Environmental Chemistry Letters*, vol. 22, pp. 2293-2318, 2024. [CrossRef] [Google Scholar] [Publisher Link]

[15] Abdullah Alkhammash, "Intelligence Analysis of Membrane Distillation via Machine Learning Models for Pharmaceutical Separation," *Scientific Reports*, vol. 14, no. 1, pp. 1-13, 2024. [CrossRef] [Google Scholar] [Publisher Link]

[16] Zhonglin Cao et al., "Machine Learning in Membrane Design: From Property Prediction to AI-Guided Optimization," *Nano Letters*, vol. 24, no. 10, pp. 2953-2960, 2024. [CrossRef] [Google Scholar] [Publisher Link]

[17] Haoyu Yin et al., "Machine Learning for Membrane Design and Discovery," *Green Energy and Environment*, vol. 9, no. 1, pp. 54-70, 2024. [CrossRef] [Google Scholar] [Publisher Link]

[18] Cody L. Ritt et al., "Machine Learning Reveals Key Ion Selectivity Mechanisms in Polymeric Membranes with Subnanometer Pores," *Science Advances*, vol. 8, no. 2, pp. 1-9, 2022. [CrossRef] [Google Scholar] [Publisher Link]

[19] Abdelfattah Amari et al., "Study of Membranes with Nanotubes to Enhance Osmosis Desalination Efficiency by Using Machine Learning towards Sustainable Water Management," *Membranes*, vol. 13, no. 1, pp. 1-18, 2023. [CrossRef] [Google Scholar] [Publisher Link]

[20] Qisong Xu et al., "Synergizing Machine Learning, Molecular Simulation and Experiment to Develop Polymer Membranes for Solvent Recovery," *Journal of Membrane Science*, vol. 678, 2023. [CrossRef] [Google Scholar] [Publisher Link]

[21] Jowaher Alanazi et al., "Application of Different Mathematical Models based on Artificial Intelligence Technique to predict the Concentration Distribution of Solute Through a Polymeric Membrane," *Ecotoxicology and Environmental Safety*, vol. 262, pp. 1-9, 2023. [CrossRef] [Google Scholar] [Publisher Link]

[22] Ali K. Shargh, and Niaz Abdolrahim, "An Interpretable Deep Learning Approach for Designing Nanoporous Silicon Nitride Membranes with Tunable Mechanical Properties," *NPJ Computational Materials*, vol. 9, pp. 1-10, 2023. [CrossRef] [Google Scholar] [Publisher Link]

[23] Mostafa Delpisheh et al., "Leveraging Machine Learning in Porous Media," *Journal of Materials Chemistry A*, vol. 12, no. 32, pp. 20717-20782, 2024. [CrossRef] [Google Scholar] [Publisher Link]

[24] Muteb Alanazi, and Tareq Nafea Alharby, "Computational Evaluation Using Machine Learning for Analysis of Membrane Desalination Process Powered by Solar Energy," *Scientific Reports*, vol. 15, no. 1, pp. 1-12, 2025. [CrossRef] [Google Scholar] [Publisher Link]

[25] Pooria Behnam et al., "Development of Machine Learning and Stepwise Mechanistic Models for Performance Prediction of Direct Contact Membrane Distillation Module – A Comparative Study," *Chemical Engineering and Processing: Process Intensification*, vol. 173, 2022. [CrossRef] [Google Scholar] [Publisher Link]

[26] Mohamed Abd Elaziz et al., "Machine Learning-Aided Modeling for Predicting Freshwater Production of a Membrane Desalination System: A Long-Short-Term Memory Coupled with Election-Based Optimizer," *Alexandria Engineering Journal*, vol. 86, pp. 690-703, 2024. [CrossRef] [Google Scholar] [Publisher Link]

[27] Bashar H. Ismael et al., "Permeation Flux Prediction of Vacuum Membrane Distillation Using Hybrid Machine Learning Techniques," *Membranes*, vol. 13, no. 12, pp. 1-19, 2023. [CrossRef] [Google Scholar] [Publisher Link]

[28] Scott Lundberg, and Su-In Lee, "A Unified Approach to Interpreting Model Predictions," *Arxiv Preprint*, pp. 1-10, 2017. [CrossRef] [Google Scholar] [Publisher Link]

[29] Ahmad S. Jawed et al., "ANN-GA Driven Prediction and Optimization for Upscaling Photothermal Air-Gap Membrane Distillation Systems using Octy-Cu/PVDF Membranes," *Journal of Environmental Chemical Engineering*, vol. 13, no. 4, pp. 1-16, 2025. [CrossRef] [Google Scholar] [Publisher Link]

[30] Lobna Nassar et al., "Optimizing Operating Parameters for the Scalability of Photothermal Membrane Distillation using Machine Learning Techniques," *Desalination*, vol. 613, pp. 1-14, 2025. [CrossRef] [Google Scholar] [Publisher Link]

[31] Isabel Requena et al., "Application of Machine Learning to Characterize the Permeate Quality in Pilot-Scale Vacuum-Assisted Air Gap Membrane Distillation Operation," *Membranes*, vol. 13, no. 11, pp. 1-21, 2023. [CrossRef] [Google Scholar] [Publisher Link]